Chemical Engineering Journal 550 (2026) 184103

Contents lists available at ScienceDirect

Chemical Engineering Journal

journal homepage: www.elsevier.com/locate/cej

Hexagonal star-like Co/CeO_2 heterostructures with interfacial electron modulation for efficient bifunctional oxygen electrocatalysis in zinc–air batteries and fuel cells

Biao Fu [a,1], Yingfang Huang [a,1], Peisen Wu [a], Ke Zhang [a], Zhiyang Huang [a], Sheraz Muhammad [a], Jiawen Huang [a], Jiajie Lin [a], Tayirjan Taylor Isimjan [b,*], Bao Wang [c,*], Xiulin Yang [a,*]

[a] Guangxi Key Laboratory of Low Carbon Energy Materials, School of Chemistry and Pharmaceutical Sciences, Guangxi Normal University, Guilin, 541004, China
[b] Saudi Arabia Basic Industries Corporation (SABIC) at King Abdullah University of Science and Technology (KAUST), Thuwal, 23955-6900, Saudi Arabia
[c] State Key Laboratory of Biochemical Engineering, Institute of Process Engineering, Chinese Academy of Sciences, Beijing, 100190, China

ARTICLE INFO

Keywords:
Co/CeO_2@NC–SL heterostructure
Interfacial electron modulation
Oxygen reduction
Zinc-air batteries
Fuel cells

ABSTRACT

The widespread adoption of rechargeable zinc-air batteries (ZABs) and fuel cells is critically hindered by the sluggish kinetics of oxygen electrocatalysis at the air cathode, while noble-metal catalysts remain economically unviable due to their high cost, scarcity, and poor durability. Herein, we present a bifunctional oxygen electrocatalyst consisting of hexagonal star-like Co/CeO_2 (Co/CeO_2@NC–SL). This material achieves an outstanding ORR half-wave potential of 0.87 V and a low OER overpotential of 318 mV at 10 mA cm^{-2}. The catalytic performance is synergistically driven by the Co−O−Ce heterointerface, which facilitates interfacial electron transfer from Co to CeO_2, thereby optimizing the electronic structure and modulating the adsorption energetics of oxygen-containing intermediates. In rechargeable aqueous ZABs, the catalyst delivers a peak power density of 191.82 mW cm^{-2} and exceptional cycling stability of ~1200 h, while AEMFCs employing it as the cathode achieve an impressive peak power density of 1261.95 mW cm^{-2}. This work elucidates the mechanistic role of Co/CeO_2 heterointerfaces in boosting bifunctional activity and offers a viable pathway toward high-performance, cost-effective electrocatalysts for sustainable energy conversion and storage systems.

1. Introduction

Rechargeable zinc-air batteries (ZABs) have emerged as up-and-coming next-generation energy conversion devices owing to their remarkable attributes, including high specific energy density, low cost, and enhanced safety [1–3]. However, the large-scale commercialization of ZABs is severely hindered by the sluggish kinetics of the oxygen reduction reaction (ORR) and oxygen evolution reaction (OER) at the cathode [4–6]. Beyond ZABs, anion exchange membrane fuel cells (AEMFCs) represent another critical platform where efficient ORR catalysts are urgently needed for hydrogen-based energy conversion, yet they face similar challenges associated with sluggish cathodic kinetics [7,8]. Although noble-metal electrocatalysts, such as Pt, RuO_2, and IrO_2 exhibit exceptional catalytic activity, their commercial application is significantly hindered by high cost, scarce resources, and poor durability [9–11]. Consequently, there is an urgent need to develop cost-effective and highly active non-noble metal catalysts. Transition-metal-nitrogen-carbon catalysts integrated with metal nanoparticles have emerged as promising alternative for high-performance bifunctional ORR/OER catalysis [12–14]. Among them, cobalt (Co)-based composites are desirable due to their abundant terrestrial reserves, favorable cost-effectiveness, and tunable electronic structures [15]. Nevertheless, the catalytic performance of Co-based materials is often constrained by insufficient exposure of active sites, limited electrical conductivity, and suboptimal adsorption energy for oxygen intermediates. These intrinsic limitations significantly restrict their long-term applicability in energy devices such as ZABs and impede practical deployment [16,17].

In recent years, interface engineering has been widely recognized as an effective strategy for enhancing electrocatalytic performance. The construction of heterostructures can regulate interfacial charge distribution and optimize the adsorption behavior of reaction intermediates key factors governing electrochemical catalysis [18]. Intimate contact

* Corresponding authors.
E-mail addresses: isimjant@sabic.com (T.T. Isimjan), baowang@ipe.ac.cn (B. Wang), xlyang@gxnu.edu.cn (X. Yang).
[1] These authors contributed equally to this work.

https://doi.org/10.1016/j.cej.2026.184103
Received 7 August 2026; Received in revised form 25 September 2026; Accepted 8 November 2026
Available online 10 November 2026
1385-8947/© 2026 Elsevier B.V. All rights are reserved, including those for text and data mining, AI training, and similar technologies.

between different active components at well-designed heterointerfaces induces strong synergistic effects, accelerates charge transfer, and optimizes the adsorption and activation energies of intermediates, thereby overcoming the limitations inherent in single-component materials [19]. Moreover, heterointerfaces often incorporate structural variations such as dislocations, stepped surfaces, grain boundaries, and atomic-scale defects including anion/cation vacancies, which collectively increase the density of catalytically active sites on the catalyst surface [20]. In particular, cerium dioxide (CeO_2) has attracted considerable attention owing to its unique oxygen storage and release capacity, which originates from the reversible Ce^{3+}/Ce^{4+} redox couple and the facile formation of oxygen vacancies [21,22]. When integrated with Co-based components, CeO_2 serves as an efficient electron modulator. Accumulating evidence confirms that interfacial electron transfer from Co to CeO_2 occurs at the Co/CeO_2 heterojunction, thereby optimizing the electronic structure of Co active sites, modulating the adsorption/desorption behavior of oxygen intermediates, and ultimately enhances the intrinsic catalytic activity. For instance, Li et al. reported that CeO_2 decorating modifies the interface, generates abundant oxygen vacancies, and alters the electronic states of CoP, thereby tuning the Co^{2+}/Co^{3+} ratio and enhancing OER catalytic activity [23].

In addition, the microstructural design of catalysts plays an equally critical role in determining their performance. An ideal architecture should feature a high specific surface area, abundant hierarchical porosity, and good hydrophilicity to facilitate mass transport, electrolyte wetting, and accessibility of active sites. For instance, three-dimensional (3D) structures, hollow structures, or open mesoporous morphologies can effectively improve mass transfer efficiency and site availability [24,25]. Nitrogen-doped carbon (NC) substrates not only enhance the electrical conductivity of composites but also synergistically optimize charge transfer with metal active sites. Despite advances in CeO_2-based electrocatalysts, the underlying mechanism of CeO_2 as an electron modulator in ZABs particularly the synergistic enhancement of dual ORR/OER performance via heterojunction formation with Co species has not yet been fully elucidated. Moreover, maximizing the electron-modulating effect of CeO_2 through precise morphology control and interfacial engineering remains an open challenge. Furthermore, while most studies focus on either ZABs or fuel cells separately, the development of a versatile ORR catalyst that performs excellently in both alkaline energy systems is highly desirable but rarely achieved. Despite considerable progress, reported Co/CeO_2 bifunctional catalysts remain confined to nanoparticles, nanorods, polyhedra, nanosheets, nanoboxes or disordered multilayers, and are almost exclusively evaluated in a single device, typically rechargeable ZABs, with no AEMFC assessment [22,26]. Moreover, in the most recent rare-earth-oxide-tailored Co-N-C catalyst [27], CeO_2 persists as a physically separate phase with no detectable Co—O bonding, so that the Co−O−Ce interfacial linkage itself remains largely unexplored.

Here we report a CTAB-directed three-dimensional hexagonal star-like Co/CeO_2 heterostructure embedded in N-doped carbon (Co/CeO_2@NC–SL), in which a genuine Co−O−Ce interface is established and verified by Co K-edge XANES/EXAFS/WT analysis together with in situ ATR-SEIRAS. We further show that this single catalyst operates efficiently in both rechargeable ZABs and AEMFCs, thereby closing the gap between half-cell bifunctionality and practical dual-device operation. The unique 3D star-like architecture not only provides a large specific surface area and hierarchical pore channels for enhanced mass transfer but also induces pronounced charge redistribution through strong electronic interactions between Co and CeO_2. Such interactions optimize the adsorption energies of oxygen intermediates, thereby promoting an efficient four-electron ORR pathway. Electrochemical tests demonstrate that the as-prepared Co/CeO_2@NC–SL catalyst exhibits an outstanding ORR half-wave potential (0.87 V) and a low OER overpotential (318 mV at 10 mA cm^{-2}). When applied in rechargeable ZABs, the Co/CeO_2@NC–SL catalyst delivers a high peak power density of 191.82 mW cm^{-2} and remarkable cycling stability approximately 1200 h. Furthermore, all-solid-state batteries fabricated with this catalyst achieve a power density of 66.40 mW cm^{-2} and maintain stable operation for approximately 100 h. Remarkably, when evaluated as the cathode catalyst in AEMFCs, Co/CeO_2@NC–SL achieves impressive peak power densities of 600.52 mW cm^{-2} under H_2-air and 1261.95 mW cm^{-2} under H_2-O_2 conditions, with robust durability. This work not only elucidates the critical role of heterointerfaces in regulating electrocatalytic performance but also provides a feasible strategy for the rational design of high performance bifunctional electrocatalysts for sustainable energy storage and conversion technologies.

2. Materials and methods

2.1. Chemicals

Cobalt (II) nitrate hexahydrate ($Co(NO_3)_2{\cdot}6H_2O$, ≥ 99%), zinc nitrate hexahydrate ($Zn(NO_3)_2{\cdot}6H_2O$, 99%), 2-methylimidazole (2-MIM, 98%), were purchased from Xilong Chemical Co., Ltd. Cerium nitrate hexahydrate ($Ce(NO_3)_3{\cdot}6H_2O$, 99.5%), cetyltrimethylammonium bromide (CTAB), and commercial Pt/C (20 wt% Pt) were obtained from Shanghai Aladdin Biochemical Technology Co., Ltd. Nafion (5% solution) was acquired from Alfa Aesar. All the above reagents were of analytical grade and used without further purification. Ruthenium dioxide (RuO_2) powder was prepared via calcination $RuCl_3{\cdot}xH_2O$ (99%, Ru 37–40%) in air at 400 °C.

2.2. Preparation of catalysts

2.2.1. Synthesis of Ce/ZiF-67 precursor

For catalyst preparation, two solutions were first prepared: solution A (20 mL deionized water containing 2 mmol $Zn(NO_3)_2{\cdot}6H_2O$, 10 mg CTAB, 0.85 mmol $Co(NO_3)_2{\cdot}6H_2O$, and 0.15 mmol $Ce(NO_3)_3{\cdot}6H_2O$) and solution B (80 mL ultrapure water with 54.8 mmol 2-MIM). The former was rapidly poured into the latter under vigorous stirring, and the mixture was kept stirring for 3 h to ensure complete reaction. The resulting solid was then filtered, sequentially rinsed with ultrapure water and ethanol (three cycles each), and dried under vacuum at 60 °C for 6 h, yielding the precursor denoted as Ce/ZiF-67. To optimize the Ce/Co ratio, a series of samples were synthesized with Ce/Co molar ratios of 0:1, 1:4, 3:17, 1:9, and 1:0, while keeping the total metal salt amount fixed at 1 mmol.

2.2.2. Synthesis of Co/CeO_2@NC–SL and Co/CeO_2@NC–DL

The Co/CeO_2@NC–SL composite was synthesized by pyrolyzing the precursor at 910 °C for 2 h under Ar flow (ramp rate: 5 °C min^{-1}), followed by natural cooling to ambient temperature. The Co/CeO_2@NC–DL was prepared identically, omitting CTAB from the synthesis.

2.3. Characterizations

Phase composition and graphitization degree were examined by X-ray diffraction (XRD, Rigaku D/Max-3c, Cu Kα, λ = 0.15418 nm) and Raman spectroscopy (Renishaw inVia Qontor). Morphological and microstructural features were probed via scanning/transmission electron microscopy (SEM, FEI Quanta FEG 200; TEM, FEI Talos F200S) coupled with energy-dispersive X-ray spectroscopy (EDX). Porosity parameters, including BET surface area and pore size distribution, were determined on a Quantachrome 3H-2000PS4 analyzer. Electron paramagnetic resonance (EPR) spectra and X-ray photoelectron spectroscopy (XPS) data were collected using Bruker A300 and Thermo ESCALAB 250Xi spectrometers, respectively. Ultraviolet photoelectron spectroscopy (UPS) was performed on a PHI 5000 Versa Probe III system. The Ag layer acted as a reference to measure the kinetic energy corresponding to the E_f and then the E_f was corrected to 0 eV. Co K-edge X-ray absorption fine structure (XAFS) spectra were acquired in transmission mode on a

laboratory-based easyXAFS300+ spectrometer (X-ray tube: 20 kV, 20 mA; bent crystal analyzers: curvature radius 500 mm, Rowland circle R = 250 mm). In situ attenuated total reflectance surface-enhanced infrared absorption spectroscopy (ATR-SEIRAS) was carried out on a Nicolet 6700 spectrometer with an MCT detector, using an Au-nanoparticle-coated Si wafer as the working electrode. Contact angles were measured using a contact angle meter (JC2000D, China). For each sample, at least three parallel measurements were performed, and the results are reported as the mean ± standard deviation.

2.4. Electrochemical measurements

ORR activity tests were performed on a CHI 760E electrochemical workstation using a three-electrode system at ambient temperature. An Ag/AgCl electrode (saturated KCl filling solution) and a graphite rod served as the reference electrode and auxiliary electrode, respectively. The working electrode was either a rotating ring-disk electrode (RRDE, diameter = 5.61 mm, PINE Instruments, USA) or a rotating disk electrode (RDE, diameter = 5 mm, PINE Instruments, USA), both loaded with catalyst ink. The catalyst ink was prepared as follows: 2 mg of the electrocatalyst was mixed with 200 μL of isopropanol, 100 μL of deionized water, and 5 μL of a 5 wt% Nafion solution. The mixture was sonicated for 2 h to achieve a homogeneous dispersion. Subsequently, 25 μL of the homogeneous catalyst ink was uniformly dropped onto the surface of the RRDE and allowed to dry naturally under ambient conditions. More detailed description of the test and calculation approaches are provided in the supplementary data.

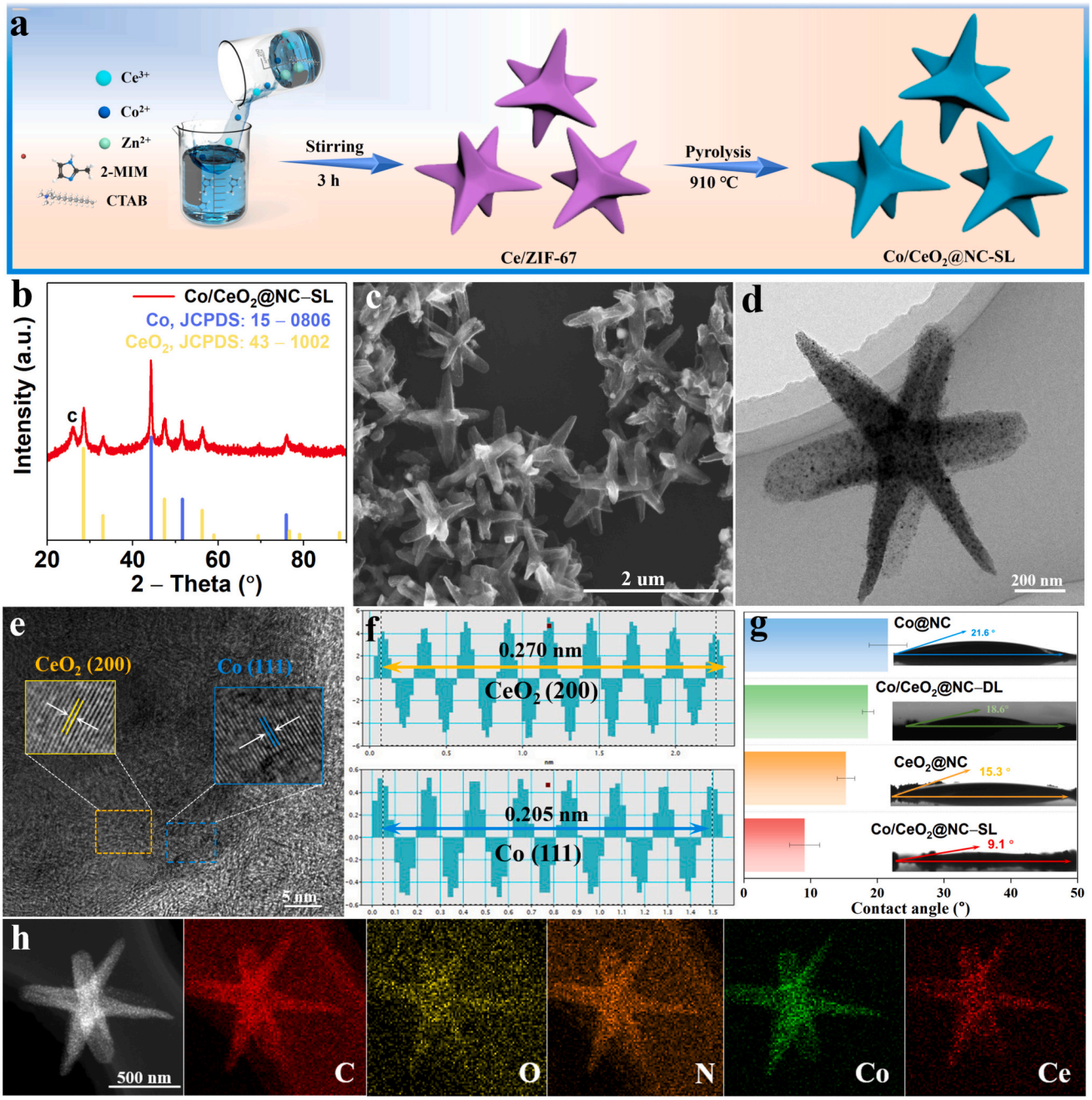


Fig. 1. (a) Schematic illustration of the synthesis process for Co/CeO_2@NC–SL. (b) XRD patterns of Co/CeO_2@NC–SL. (c) SEM, (d) TEM, (e) HR-TEM images and the lattice spacing profiles. (f) The FFT pattern from (e). (g) Contact angle measurements of different catalysts. (h) HAADF-STEM image and corresponding elemental mapping results for Co/CeO_2@NC–SL.

3. Results and discussion

Fig. 1a illustrates the synthesis procedure of Co/CeO_2@NC–SL with star-like morphology, which involves the metal-organic framework construction, surfactant-assisted morphology control, and in situ metal ion exchange technologies. Initially, Zn^{2+} ions and 2-methylimidazole were assembled to form the ZIF-8 and ZIF-L complexes. Subsequently, upon the introduction of Co^{2+} and Ce^{3+} ions, partial Zn^{2+} ions were replaced by Co^{2+} and Ce^{3+} ions, yielding a hexagonal carbonaceous precursor. After pyrolysis at 910 °C under an Ar atmosphere, this precursor was converted into Co/CeO_2@NC–SL. For comparison, the Co/CeO_2@NC–DL was synthesized following the same procedure but without the addition of CTAB. X-ray diffraction (XRD) analysis was performed to identify the crystalline structures of the as-prepared catalysts. As shown in Figs. 1b and S1, the diffraction peaks at 44.2°, 51.5°, and 75.9° are well indexed to metallic Co (JCPDS: 15–0806) [28], and the remaining peaks, except for the carbon diffraction peak at 26.0°, can be perfectly assigned to CeO_2 (JCPDS: 43–1002) [29,30]. Meanwhile, the Co@NC and CeO_2@NC predominantly consist of the Co and CeO_2 crystalline phases, respectively.

The structural morphologies of the as-prepared samples were characterized using scanning electron microscopy (SEM) and transmission electron microscopy (TEM). As shown in Figs. 1c, d, and S2, both the precursor and Co/CeO_2@NC–SL exhibit a 3D hexagonal star shape, indicating high structural stability. In contrast, Co/CeO_2@NC–DL displays a polyhedral morphology, as shown in Fig. S3, demonstrating that CTAB plays a role in regulating the catalyst morphology. High-resolution transmission electron microscopy (HR-TEM) images (Figs. 1e and f) reveal lattice spacings of 0.270 and 0.205 nm, corresponding to the (200) crystal plane of CeO_2 and the (111) crystal plane of Co, respectively, confirming the formation of CeO_2/Co heterostructures. Such unique interface structures can modulate the electronic properties of the metal centers and enhance electrochemical reaction kinetics [31]. As shown in Fig. 1g, Co/CeO_2@NC–SL exhibits a contact angle of 9.1°, which is markedly lower than those of Co@NC (21.6°), CeO_2@NC (15.3°), and Co/CeO_2@NC–DL (18.6°), demonstrating significantly enhanced hydrophilicity [32]. This improved wettability stems from the synergistic integration of CeO_2 and Co within the heterointerface, combined with the unique 3D star-like morphology engineered through CTAB regulation. The highly hydrophilic surface promotes electrolyte penetration into the catalyst pores and improves the accessibility of active sites, thereby facilitating ORR kinetics

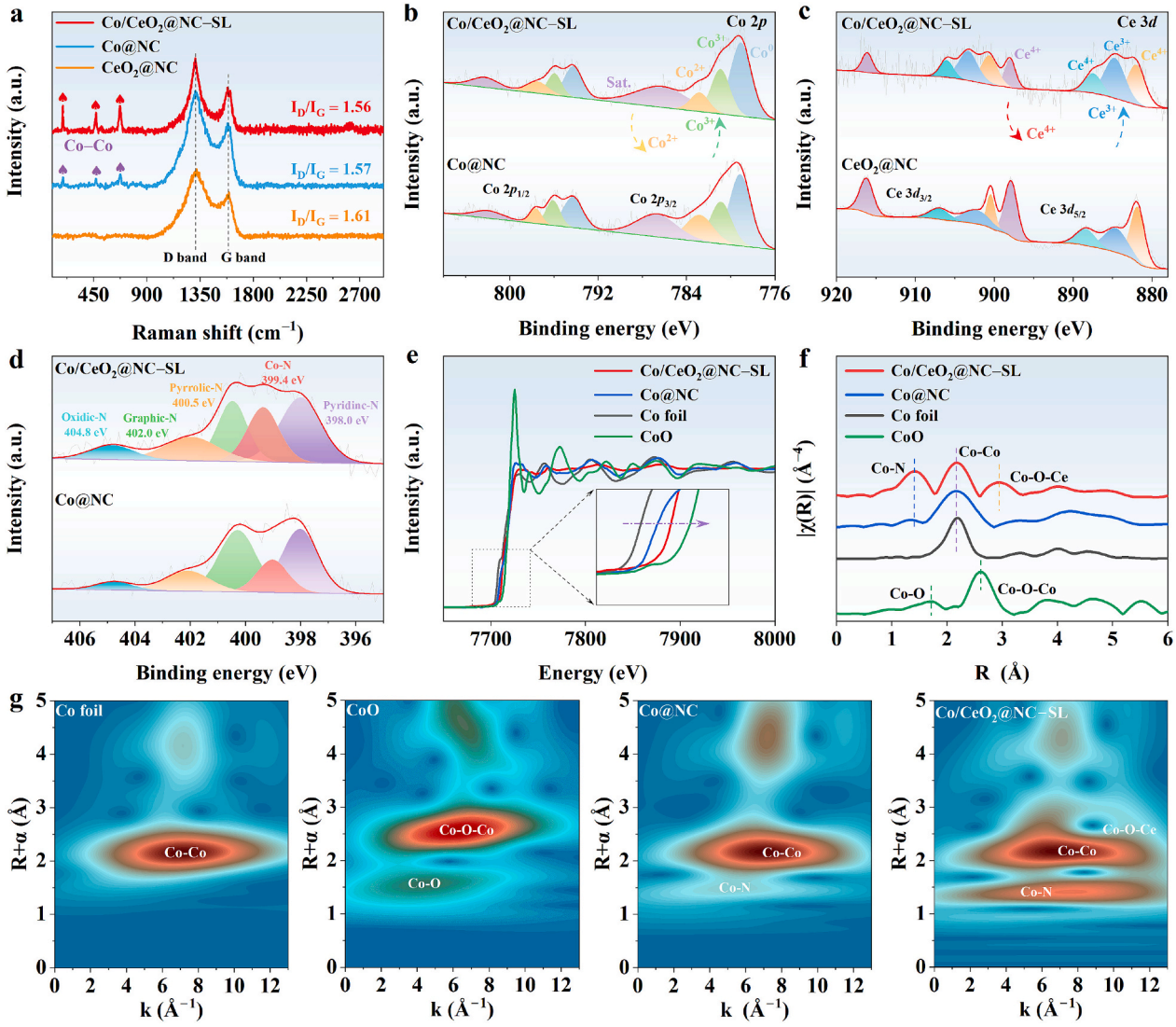


Fig. 2. (a) Raman spectra of Co/CeO_2@NC–SL, Co@NC, and CeO_2@NC. High-resolution XPS spectra of (b) Co 2*p*, (c) Ce 3*d*, and (d) N 1*s* for Co/CeO_2@NC–SL, CeO_2@NC and Co@NC. (e) Co K-edge XANES spectra of Co/CeO_2@NC–SL, Co@NC, Co foil, and CoO. (f) Co K-edge FT-EXAFS spectra of Co/CeO_2@NC–SL, Co@NC, Co foil, and CoO. (g) Co K-edge WT-EXAFS contour plots of Co/CeO_2@NC–SL, Co@NC, Co foil, and CoO.

[33,34]. High-angle annular dark-field scanning transmission electron microscopy (HAADF-STEM) along with elemental mapping revealed a homogeneous elemental distribution of C, O, N, Co and Ce (Fig. 1h), validating the successful fabrication of Co/CeO_2@NC–SL.

To further investigate the local structural features, Raman spectroscopy was carried out. As shown in Fig. 2a, Raman spectroscopy analysis indicated the presence of Co—Co dominant vibrational modes within the Co/CeO_2@NC–SL and Co@NC samples. Specifically, these modes were detected at 193, 476, and 688 cm^{-1}, respectively [35]. The D band (defective carbon) and G band (graphitized carbon) were observed at 1316 and 1590 cm^{-1}, respectively [36]. The peak intensity ratios (I_D/I_G) serve as indicators of the defect degree and graphitization level within carbon-based catalysts [37]. The peak intensity ratios of I_D/I_G for Co/CeO_2@NC–SL, Co@NC, and CeO_2@NC catalysts are 1.56, 1.57, and 1.61, respectively, suggesting a slight enhancement in graphitization upon CeO_2 incorporation and thus improved electrical conductivity of the material. X-ray photoelectron spectroscopy (XPS) was employed to gain information on the elemental composition and the oxidation states of the catalysts.

The XPS survey spectrum of Co/CeO_2@NC–SL (Fig. S4) confirms the presence of Co, Ce, C, N, and O, consistent with the element mapping results. The high resolution C 1*s* spectrum (Fig. S5) can be deconvoluted into four peaks corresponding to C═C (284.0 eV), C—C (284.8 eV), C—O/C—N (286.0 eV), and C═O (288.5 eV) [38]. As shown in Fig. 2b, the Co 2*p* spectrum can be deconvoluted into Co^0 (779.1/794.2 eV), Co^{3+} (780.9/795.9 eV), Co^{2+} (782.8/797.5 eV), and the corresponding satellite peaks (786.2/802.3 eV) of Co $2p_{3/2}$ and Co $2p_{1/2}$, respectively [16,31]. In the Ce 3*d* spectrum of Co/CeO_2@NC–SL (Fig. 2c), four pairs of spin-energy split peaks are identified. Among them, the peaks centered at 885.0 and 903.4 eV are assigned to Ce^{3+} (Ce $3d_{5/2}$ and Ce $3d_{3/2}$), while the remaining peaks are assigned to Ce^{4+} [39,40]. Notably, the Co^{3+}/Co^{2+} peak-area ratio increases from 1.75 in Co@NC to 2.36 in Co/CeO_2@NC–SL, whereas the Ce^{4+}/Ce^{3+} ratio decreases markedly from 3.22 to 1.64 upon CeO_2 incorporation. This synchronous variation in valence state ratios is attributed to the interfacial electron transfer process, where electrons are transferred from Co species to CeO_2. As an effective electronic regulator, CeO_2 possesses abundant 4*f* orbitals capable of accommodating unpaired electrons [41]. As displayed in Fig. 2d, the N 1*s* spectrum of Co/CeO_2@NC–SL can be deconvoluted into four peaks, corresponding to pyridinic-N, Co—N, pyrrolic-N, graphitic-N and oxidized-N, respectively [42].

To further verify the valence state and coordination environment of Co, Co K-edge X-ray absorption spectroscopy (XAS) measurements were performed. The near-edge (XANES) and extended fine structure (EXAFS) spectra, combined with wavelet transform (WT) analysis, were utilized to assess the atomic structure and distinguish the backscattering atoms around the Co centers. Because WT resolves the EXAFS signal simultaneously in radial distance (R) and wavenumber (k) space, it enables discrimination of backscattering atoms by their elemental nature even at similar distances, with heavier scatterers appearing at higher k values [43], WT therefore permits reliable identification of the coordination environment through the k-resolved contribution of each scattering path [44]. The near-edge (XANES) and extended fine structure (EXAFS) spectra, combined with wavelet transform (WT) analysis, were utilized to qualitatively assess the atomic structure and distinguish the backscattering atoms around the Co centers. As shown in Fig. 2e, the pre-edge region of the Co K-edge XANES spectrum of Co/CeO_2@NC–SL is positively shifted relative to that of Co@NC, indicating a higher Co oxidation state upon CeO_2 incorporation. This observation implies pronounced electron transfer from Co to Ce, with Ce sites acting as electron acceptors, which is in good agreement with the XPS results. The Fourier-transformed (FT) EXAFS spectra (Fig. 2f) provide direct insight into the coordination environment. For Co/CeO_2@NC–SL, three distinct FT peaks are observed at the apparent radial distances (without phase correction) of approximately 1.42, 2.17, and 2.95 Å, whereas Co@NC exhibits only the first two peaks. To unambiguously identify the nature of the backscattering atoms responsible for these FT peaks—especially the additional feature at ~2.95 Å—we performed WT analysis (Fig. 2g). In the WT contour plots, both Co@NC and Co/CeO_2@NC–SL display a WT maximum at ~1.4 Å, confirming the presence of Co—N coordination in both samples, which is consistent with the Co—N peak observed in the XPS N 1*s* spectrum. At the radial distance of ~2.17 Å, Co@NC shows only a single WT maximum at ~7.0 $Å^{-1}$, a characteristic signature of the Co—Co metallic path. In stark contrast, Co/CeO_2@NC–SL exhibits an additional WT maximum at a higher k-value region (beyond 7.0 $Å^{-1}$) within the radial of ~2.95 Å. Given that heavier atoms (such as Ce) exhibit stronger backscattering at higher k values compared to lighter Co atoms, this distinct WT feature is characteristic of the Co—O—Ce scattering path. Importantly, this additional WT feature is completely absent in Co@NC, unequivocally demonstrating that the Co—O—Ce interfacial connectivity arises solely from the introduction of CeO_2. Collectively, the combination of XANES (positive edge shift), FT-EXAFS (emergence of a new peak at ~2.95 Å), and WT (a high-k backscattering feature characteristic of the heavier Ce scatterer) consistently provides compelling evidence for the formation of a robust Co—O—Ce heterointerface between Co and CeO_2, which serves as the key structural motif responsible for the enhanced bifunctional electrocatalytic performance of Co/CeO_2@NC–SL.

Beyond the intrinsic interfacial electron modulation, the structural advantages of the CTAB-tailored 3D star-like architecture are primarily reflected in its well-developed hierarchical pore structure, which facilitates mass transport and improves the accessibility of active sites. Co/CeO_2@NC–SL exhibits a specific surface area of 331.25 $m^2\ g^{-1}$, only slightly higher than that of Co/CeO_2@NC–DL (307.12 $m^2\ g^{-1}$) (Figs. 3a and S6). It is important to note that this modest increase in surface area is insufficient to account for the drastically enhanced catalytic activity; rather, the performance is primarily governed by the interfacial electron modulation at the Co—O—Ce heterointerface, as evidenced by the spectroscopic characterizations discussed above. Instead, the CTAB-tailored 3D hexagonal star structure serves as a crucial auxiliary factor by providing well-developed mesoporosity (average pore size 6.4 nm), which effectively accelerates mass transport during the ORR process and improves the accessibility of the active sites, thereby facilitating the macroscopic ORR performance alongside the intrinsic electronic effects [45,46]. More importantly, to further elucidate the intrinsic origin of the enhanced activity beyond textural contributions, the energy band structures of the as-prepared catalysts were analyzed via ultraviolet photoelectron spectroscopy (UPS), as shown in Fig. 3b. The cutoff energies (E_{cutoff}) of Co/CeO_2@NC–SL and Co@NC are determined to be 16.37 and 16.23 eV, corresponding to work functions of 4.85 and 4.99 eV.

The reduced work function (WF) of Co/CeO_2@NC–SL facilitates the rapid transfer of electrons from the catalyst interior to the surface, as well as efficient electron exchange with the reactants, thereby enhancing their interaction with the reactants [47]. This enhanced electron mobility not only strengthens the interaction between the catalyst and reactants but also lays a favorable foundation for accelerating the kinetics of electrocatalytic reactions. Moreover, the valence band maxima (VBM) of Co/CeO_2@NC–SL and Co@NC are detected at 3.25 and 3.46 eV, respectively (Fig. 3c). Compared with Co@NC, the valence band of Co/CeO_2@NC–SL is closer to the Fermi level, indicating that CeO_2 incorporation induces an upward shift of the valence band and effectively enhances the electrical conductivity of the catalyst [48]. Consistent with the XPS and XANES finding that CeO_2 serves as an electron acceptor, the energy band diagram in Fig. 3d schematically illustrates a built-in electric field that drives unidirectional electron transfer from Co to CeO_2. This charge redistribution creates an electron-rich CeO_2 region and an electron-deficient Co region, thereby balancing local charge and optimizing the adsorption of oxygen intermediates [49,50].

Furthermore, the potential of zero charge (PZC) of catalysts was obtained by using the Gouy-Chapman capacitance minimum method

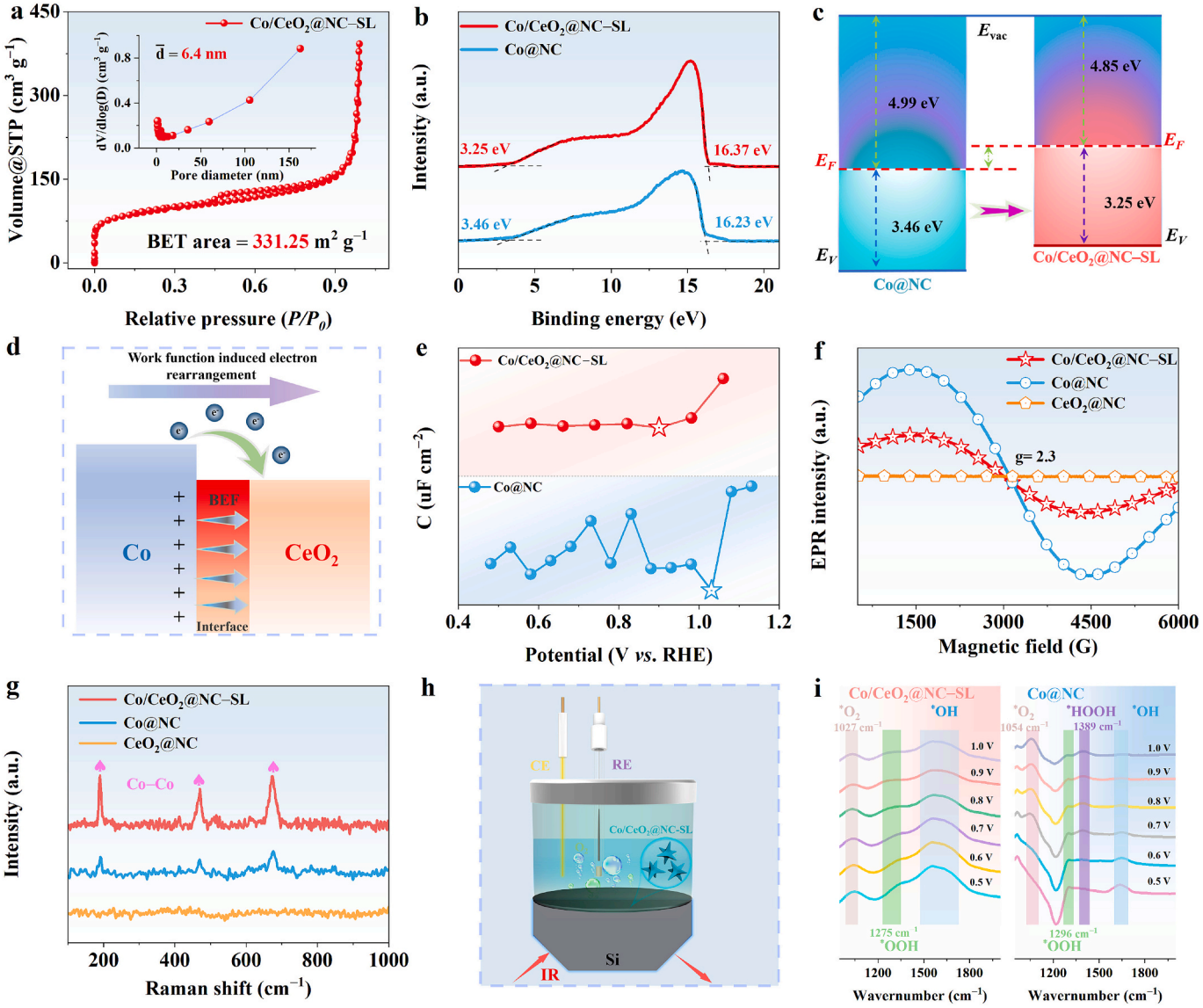


Fig. 3. Physicochemical characterization of the as-prepared catalysts. (a) N_2 adsorption-desorption isotherms of Co/CeO_2@NC–SL; the corresponding pore size distribution curve is shown in the inset. (b) UPS spectra. (c) Energy band structure alignment of Co/CeO_2@NC–SL and Co@NC. (d) Schematic illustration of the charge transfer process in Co/CeO_2@NC–SL. (e) PZC measurements conducted via the Gouy-Chapman capacitance minimum method for Co/CeO_2@NC–SL and Co@NC. (f) EPR spectra. (g) Raman spectra in the range of 450–650 cm^{-1} for Co/CeO_2@NC–SL, Co@NC, and CeO_2@NC. (h) Schematic illustration of in situ ATR-SEIRAS setup. (i) In situ ATR-SEIRAS spectra of Co/CeO_2@NC–SL and Co@NC recorded during ORR testing in O_2-saturated 0.1 M KOH.

[51]. As shown in Fig. 3e, the PZC value of Co/CeO_2@NC–SL (0.90 V) is smaller than that of Co@NC (1.03 V). These results show the same trend as the WF results, which is due to the positive correlation between WF and PZC [52]. Fig. 3f presents the electron paramagnetic resonance (EPR) spectra, where Co/CeO_2@NC–SL displays a markedly weaker signal intensity compared to Co@NC. This attenuation indicates that the introduction of CeO_2 induces localized electronic rearrangements, facilitating electron transfer from Co species to CeO_2. The interfacial charge redistribution modulates the electronic structure of the Co active sites. This optimization simultaneously improves the charge transport kinetics within the material and adjusts the adsorption of intermediates, synergistically enhancing the overall catalytic performance. Crucially, complementary Raman spectroscopy provides key insight into the origin of this EPR signal. As shown in Fig. 3g, neither Co/CeO_2@NC–SL nor pure CeO_2@NC exhibits a characteristic Raman peak near 600 cm^{-1}, a region often associated with signals from certain oxygen vacancy defects in CeO_2 [53]. The absence of this peak suggests that intrinsic oxygen vacancies in the CeO_2 lattice do not contribute significantly to the paramagnetic signal observed in EPR. Therefore, the pronounced change in the EPR signal upon forming the heterostructure can be primarily attributed to the altered electronic environment of the Co species, directly corroborating the occurrence of interfacial electron transfer.

To elucidate the reaction mechanism, in situ attenuated total reflection surface-enhanced infrared absorption spectroscopy (ATR-SEIRAS) was conducted. As depicted in Figs. 3h and i, the band around 1630 cm^{-1} is assigned to the O—H stretching vibration of water molecules, while the peaks at 1027 and 1275 cm^{-1} are attributed to the *O_2 and *OOH intermediates, respectively [54,55]. In contrast, in situ ATR-SEIRAS spectra of Co@NC reveal the emergence of a new peak (1389 cm^{-1}), which is assigned to the *HOOH bending vibration of adsorbed hydroperoxide ($HOOH_{ad}$) [56]. Collectively, these results confirm that Co/CeO_2@NC–SL exhibits excellent selectivity, favoring an efficient four-electron reduction pathway for the ORR. Furthermore, the red-shift observed in the *O_2 and *OOH absorption bands of Co/CeO_2@NC–SL, compared to those of Co@NC (1054 and 1296 cm^{-1}), indicates a more favorable interaction between the Co active sites and

oxygen intermediates upon CeO_2 doping, facilitating O—O bond cleavage [57]. These spectroscopic insights, from UPS through EPR to in situ ATR-SEIRAS, consistently demonstrate that CeO_2 acts as an electron acceptor, withdrawing electrons from Co and thereby optimizing the adsorption strength of key oxygen intermediates through the robust Co−O−Ce heterointerface. This interfacial electronic modulation is the primary origin of the enhanced bifunctional activity.

The electrocatalytic activity of the as-prepared catalysts was evaluated using a rotating disk electrode (RDE) in O_2-saturated 0.1 M KOH at room temperature. All potentials were referenced to the reversible

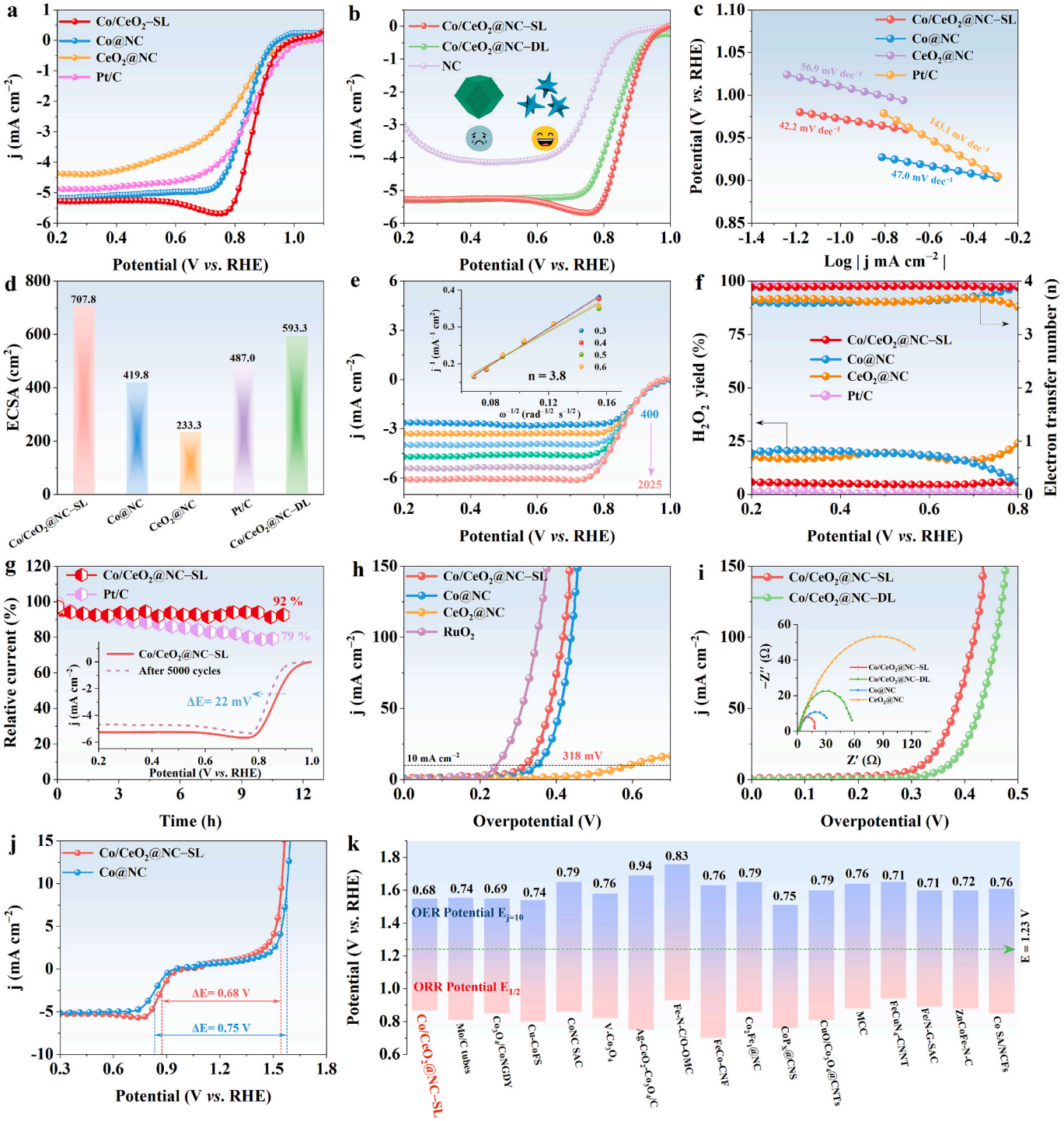


Fig. 4. Electrocatalytic performance of the prepared catalysts. (a, b) LSV polarization curves. (c) Tafel plots of different catalysts in O_2-saturated 0.1 M KOH electrolyte solution. (d) Corresponding ECSA for Co/CeO_2@NC–SL, Co/CeO_2@NC–DL, Co@NC, CeO_2@NC, and Pt/C. (e) Polarization curves of Co/CeO_2@NC–SL at rotating speeds from 400 to 2025 rpm, with corresponding K-L plots shown in the inset. (f) H_2O_2 yield and electron transfer number during the ORR. (g) Stability evaluation of Co/CeO_2@NC–SL and Pt/C (20 wt%) in 0.1 M KOH at a rotating speed of 1600 rpm (inset: polarization curves of Co/CeO_2@NC–SL recorded before and after 5000 CV cycles). OER performance of electrocatalysts in 1.0 M KOH: (h) LSV polarization curves. (i) LSV polarization curves of Co/CeO_2@NC–SL, Co/CeO_2@NC–DL (inset: Nyquist plots of electrocatalysts). (j) Combined ORR and OER LSV polarization curves of Co/CeO_2@NC–SL and Co@NC. (k) Comparison of the potentials for $E_{j=10}$ of OER, $E_{1/2}$ of ORR, and ΔE between OER and ORR with reported bifunctional catalysts.

hydrogen electrode (RHE). Systematic optimization of the Co/Ce molar ratio and annealing temperature identified Co/CeO_2@NC–SL (Co/Ce = 0.85:0.15, 910 °C) as the optimal ORR electrocatalyst (Figs. S7 and S8). As shown in Fig. S9, Co/CeO_2@NC–SL exhibits a more prominent cyclic voltammetry (CV) measurements compared with Co@NC, CeO_2@NC, and NC, indicating superior ORR activity. Consistently, linear sweep voltammetry (LSV) measurements in Fig. 4a reveal that Co/CeO_2@NC–SL delivers an excellent ORR performance with a half-wave potential ($E_{1/2}$) of 0.87 V and a limiting current density (j_L) of 5.28 mA cm^{-2}, outperforming Co@NC and CeO_2@NC and comparable to that of Pt/C. Moreover, Fig. 4b shows that Co/CeO_2@NC–SL has higher ORR activity than Co/CeO_2@NC–DL, indicating that CTAB-assisted morphology regulation effectively increases the specific surface area, exposes more active sites, and enhances oxygen reduction performance. Notably, Co/CeO_2@NC–SL exhibits faster ORR kinetics, as evidenced by a smaller Tafel slope of 42.2 mV dec^{-1}, which is substantially lower than those of Co@NC (47.0 mV dec^{-1}), CeO_2@NC (143.1 mV dec^{-1}), and Pt/C (56.9 mV dec^{-1}) (Fig. 4c). To assess intrinsic activity, the electrochemically active surface area (ECSA) was calculated based on the double-layer capacitance (C_{dl}) (Fig. S10). The ECSA of Co/CeO_2@NC-SL reaches 707.8 cm^2, significantly exceeding those of Co@NC (419.8 cm^2), CeO_2@NC (233.3 cm^2), and Co/CeO_2@NC–DL (593.3 cm^2) indicating that the unique 3D hexagonal star structure provides abundant accessible active sites to promote ORR activity (Fig. 4d). Furthermore, CV measurements in a mixed solution of 0.1 M KCl and 0.5 mM $K_3[Fe(CN)_6]$ at various scan rates (Fig. S11) yield fitting lines consistent with the C_{dl} trend, further corroborating the high accessibility of active sites in Co/CeO_2@NC–SL. To gain deeper insight into the ORR pathway, polarization curves were measured at various rotation speeds ranging from 400 to 2025 rpm (Fig. 4e).

The corresponding Koutecky-Levich (K-L) plots reveal an electron transfer number (n) close to 4, confirming that the ORR predominantly follows a four-electron transfer pathway [58]. Rotating ring-disk electrode (RRDE) measurements (Fig. 4f) further support this conclusion; among Co/CeO_2@NC–SL, Co@NC, and CeO_2@NC, the Co/CeO_2@NC–SL catalyst exhibits the lowest H_2O_2 yield (< 10%) ranging from 0.2 to 0.8 V, comparable to that of Pt/C. This result demonstrates effective suppression of peroxide formation and is fully consistent with the in situ infrared spectroscopic findings, providing mutually reinforcing evidence for the high selectivity toward the direct four-electron ORR.

Catalyst durability is another critical parameter for assessing the electrochemical performance. Chronoamperometric tests were conducted to evaluate the long-term operational stability (Figs. 4g and S12). Co/CeO_2@NC–SL retains 92% of initial current after 10 h of continuous operation, outperforming the Pt/C (79%) and Co@NC (70%). The enhanced stability of Co/CeO_2@NC–SL relative to Co@NC is attributed to the strong electronic interaction at the Co/CeO_2 heterointerface, which not only optimizes intermediate adsorption but also stabilizes the Co active sites against oxidation. Accelerated CV cycling tests further confirm its robust durability; after 5000 cycles, the $E_{1/2}$ of Co/CeO_2@NC–SL shifts negatively by only 22 mV. Furthermore, the methanol tolerance of the Co/CeO_2@NC–SL catalyst was evaluated by chronoamperometric measurements upon the addition of 3 M methanol into the electrolyte (Fig. S13). Notably, Co/CeO_2@NC–SL shows negligible current decay after methanol injection, whereas the Pt/C catalyst exhibits a pronounced sharp decrease, indicating the superior methanol resistance of our heterostructured catalyst due to its high ORR selectivity and stable active sites. Post-stability XRD analysis (Fig. S14) verifies that both Co and CeO_2 phases remain intact without detectable compositional changes. To further directly evaluate the morphological and interfacial stability, post-stability SEM and HR-TEM characterizations were performed (Fig. S15). As shown in Fig. S15a, although partial agglomeration is observed on the surface after the durability test, the overall hexagonal star-like framework is largely preserved. More importantly, the HR-TEM image and corresponding line-scan intensity profiles (Fig. S15b, c) clearly identify the lattice fringes of Co (111) and CeO_2 (220), directly confirming the retention of the Co/CeO_2 heterointerface. HAADF-STEM and elemental mapping (Fig. S15d) further reveal that despite partial agglomeration causing localized concentration, the Co, Ce, N, and O elements remain co-localized.

As the reverse process of the four-electron ORR, the OER is equally essential for rechargeable ZABs, where efficient reversibility between ORR and OER is crucial for cyclic energy conversion and storage. Accordingly, the OER performance of Co/CeO_2@NC–SL was systematically evaluated. As shown in the LSV curves (Figs. 4h and i), Co/CeO_2@NC–SL exhibits markedly superior OER activity to Co@NC, CeO_2@NC, and Co/CeO_2@NC–DL. Specifically, it requires an overpotential of only 318 mV to reach a current density of 10 mA cm^{-2}. Moreover, Co/CeO_2@NC–SL exhibits a smaller Tafel slope (Fig. S16), indicating maximized reaction kinetic, and the smallest charge transfer resistance (R_{ct}), demonstrating that its unique heterostructure effectively reduces interfacial impedance and promotes electron transfer. The potential difference ΔE, defined as the gap between the OER overpotential at current density of 10 mA cm^{-2} ($E_{j=10}$) and the ORR $E_{1/2}$, serves as a key indicator for evaluating the bifunctional catalytic activity toward ORR and OER. As presented in Fig. 4j, Co/CeO_2@NC–SL achieves a ΔE value of 0.68 V, superior to that of Co@NC (0.74 V), underscoring its excellent bifunctionality. Furthermore, a comprehensive comparison with recently reported bifunctional catalysts (Fig. 4k and Table S1) confirms that Co/CeO_2@NC–SL ranks among the most competitive non-precious metal electrocatalysts to date.

Building upon the excellent bifunctional ORR/OER activity of Co/CeO_2@NC–SL discussed above, rechargeable ZAB was assembled with Co/CeO_2@NC–SL serving as the air cathode (Fig. 5a). Notably, the open-circuit voltage (OCV) of the Co/CeO_2@NC–SL-based ZAB reaches 1.57 V, which is higher than that of the Pt/C (1.47 V) and Co@NC (1.4 V) (Figs. 5b and S17). Charge-discharge polarization curves of the ZAB was recorded at current densities ranging from 0 to 250 mA cm^{-2}, as presented in Fig. 5c. Compared with the ZAB using Pt/C + RuO_2 as the cathode catalyst, the Co/CeO_2@NC–SL-based ZAB exhibits a smaller voltage gap during the charge-discharge process, an observation that further confirms the superior integrated ORR/OER activity of the Co/CeO_2@NC–SL air cathode [59]. Furthermore, the Co/CeO_2@NC–SL-based ZAB achieves a peak power density of up to 191.82 mW cm^{-2}, which significantly surpasses that of the Pt/C-based ZAB (135.34 mW cm^{-2}). but also exceeding those of Co@NC and Co/CeO_2@NC-DL (Figs. 5d and S18). To further evaluate the practical application potential of Co/CeO_2@NC–SL, long-term galvanostatic charge-discharge cycling tests were conducted.

As shown in Fig. 5e, the Co/CeO_2@NC–SL-based ZAB maintains excellent cycling stability for around 1200 h at a current density of 5 mA cm^{-2}, demonstrating remarkable long-term operational durability. Notably, the Co/CeO_2@NC–SL system achieves a round-trip efficiency of 42.4% in its final hour over 1200 h—nearly five times longer than Pt/C—which closely matches the 45.3% of Pt/C at its end-of-life (252 h). More critically, the polarization behavior further demonstrates its superior stability: while the ΔE of Pt/C severely increases from 0.7 to 1.18 V (a 0.48 V rise), the ΔE of Co/CeO_2@NC–SL only grows from 1.16 to 1.29 V (a mere 0.13 V rise). This occurs despite a brief, beneficial activation dip to 1.12 V at 600 h. Such minimal voltage fluctuation and high terminal efficiency strongly highlight its exceptional long-term durability. This cycling stability surpasses that of most reported ZAB (Fig. 5f and Table S2), highlighting the practical advantage of our heterostructure catalyst. Galvanostatic discharge measurements were also performed to assess the rate capability of the Co/CeO_2@NC–SL-based ZAB (Fig. S19) [60,61]. The discharge voltage remains stable over a wide range of current densities (2–100 mA cm^{-2}) and fully recovers to its initial value when the current density is reduced back to 2 mA cm^{-2}. Notably, even after high-rate discharge at significant current densities, the discharge voltage completely returns to its original level at 2 mA cm^{-2}, highlighting the excellent reversibility of the Co/CeO_2@NC–SL-

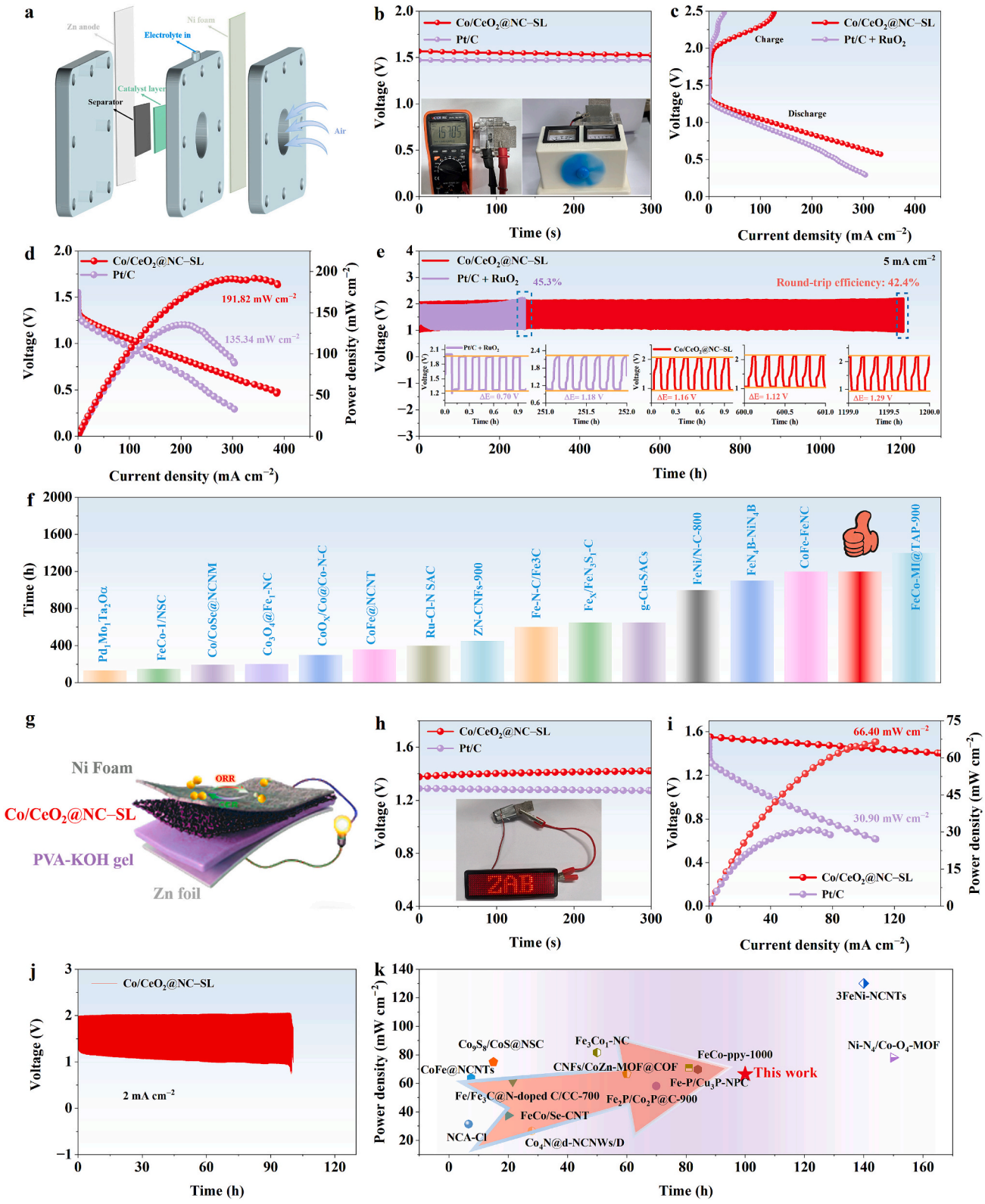


Fig. 5. Performance evaluation of Co/CeO_2@NC–SL in ZABs. (a) Schematic illustration of the assembled aqueous ZAB configuration. (b) OCV plots; the inset shows a photograph of the OCV measurement using a multimeter. (c) Charge-discharge polarization curves and (d) corresponding power density profiles of the aqueous ZAB. (e) Galvanostatic charge-discharge cycling performance at a current density of 5 mA cm^{-2} with a cycling period of 20 min per cycle. (f) Comparison of the long-term cycling stability with previously reported rechargeable ZABs. (g) Schematic illustration of the flexible ZAB configuration. (h) OCV comparison between Co/CeO_2@NC–SL and Pt/C-based cathodes. (i) Corresponding power density curves of the flexible ZABs. (j) Galvanostatic cycling performance at 2 mA cm^{-2}. (k) Comparative summary of peak power density and long-term cycling performance of flexible ZABs reported in the literature.

based ZAB. Furthermore, all-solid-state ZAB was assembled using Co/CeO_2@NC–SL as the cathode catalyst, and their schematic configuration is illustrated in Fig. 5g. As shown in Fig. 5h, the Co/CeO_2@NC–SL-based solid-state ZAB exhibits an OCV of 1.38 V, exceeding that of the Pt/C-based solid-state ZAB (1.29 V). Discharge polarization curves (Fig. 5i) reveal that the Co/CeO_2@NC–SL-based solid-state ZAB achieves a power density of 66.40 mW cm^{-2}, which is significantly higher than that of the Pt/C-based counterpart (30.90 mW cm^{-2}). In addition, the Co/CeO_2@NC–SL-based solid-state ZAB demonstrates stable cycling for approximately 100 h at a current density of 2 mA cm^{-2} (Fig. 5j).

To further evaluate the mechanical flexibility and robustness of the Co/CeO_2@NC–SL-based flexible ZAB, the OCV and power density were measured at different bending angles (0°, 30°, 60°, 90°, and 180°). As shown in Fig. S20, the OCV remains stable at 1.438–1.450 V over the entire bending range, with only a ~ 0.8% variation. The discharge polarization and power density curves (Fig. S21) show peak power densities of 60.00, 64.33, 69.26, and 65.72 mW cm^{-2} at 30°, 60°, 90°, and 180°, respectively. Notably, the peak power density at 180° retains ~99% of its flat-state value (66.40 mW cm^{-2}), indicating excellent bending tolerance. As summarized in Fig. 5k, the Co/CeO_2@NC–SL-based flexible ZAB exhibits a peak power density of 66.40 mW cm^{-2} and a cycling stability of ~100 h, both of which rank among the best values reported for flexible solid-state ZABs. This further confirms the advantage of our heterostructured catalyst over existing systems.

These results collectively establish Co/CeO_2@NC–SL as a highly efficient and durable ORR catalyst for ZABs, prompting us to explore its applicability in other alkaline energy conversion systems. Given that the cathodic oxygen reduction reaction in alkaline media underpins both rechargeable ZABs and AEMFCs, we reasoned that the unique interfacial electron modulation and optimized intermediate adsorption conferred by the Co/CeO_2 heterojunction should translate into comparable advantages in fuel cell devices. To validate this hypothesis and further expand the application scope of our catalyst, we proceeded to evaluate its performance as the cathode in a practical AEMFC setup. Fig. 6a illustrates the schematic configuration of the AEMFC employing Co/CeO_2@NC–SL as the cathode catalyst. As shown in Fig. 6b, the AEMFC equipped with Co/CeO_2@NC–SL delivered peak power densities of 600.52 mW cm^{-2} under H_2-air conditions and 1261.95 mW cm^{-2} under H_2-O_2 conditions. The high power density can be attributed to the unique 3D star-like architecture with hierarchical porosity, which facilitates efficient mass transport, coupled with the heterojunction-induced electronic modulation that optimizes the ORR kinetics at the cathode.

To assess the operational durability of Co/CeO_2@NC–SL in fuel cell environments, we conducted chronoamperometric measurements at a constant voltage of 0.70 V (Fig. 6c). The current density retained 87.3% of its initial value after 10 h of continuous operation, demonstrating exceptional stability under the combined chemical and electrochemical stresses of a working fuel cell. This robust durability underscores the structural integrity imparted by the heterojunction design and the protective nitrogen-doped carbon matrix. Furthermore, we benchmarked the peak power density of our Co/CeO_2@NC–SL-based AEMFC against recently reported metal-free and transition metal-based AEMFCs (Fig. 6d and Table S3). The superior performance of our catalyst positions it among the most promising non-precious metal ORR electrocatalysts for alkaline fuel cell applications, highlighting the effectiveness of our heterostructure engineering strategy.

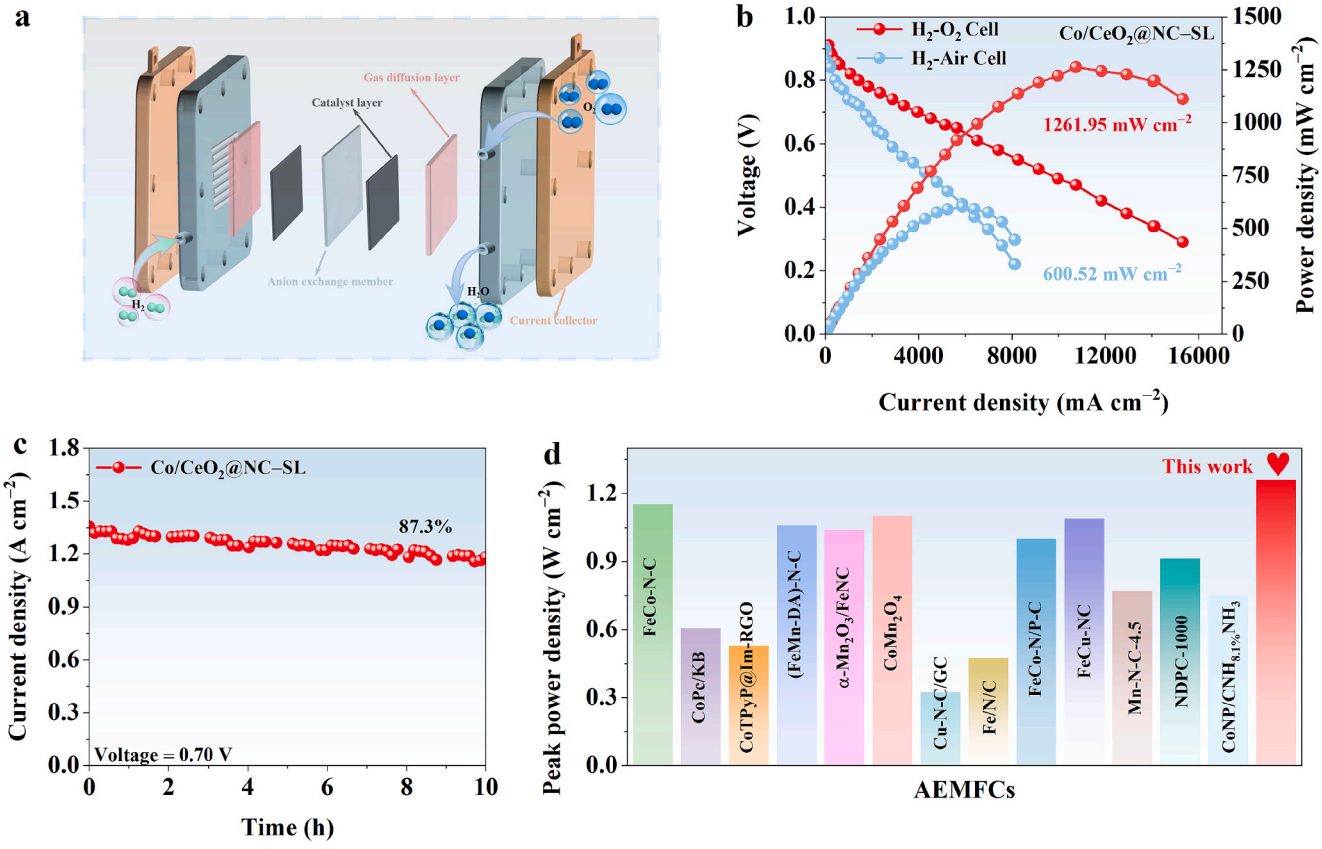


Fig. 6. Electrochemical performance evaluation of Co/CeO_2@NC–SL in an AEMFC. (a) Schematic illustration of the AEMFC configuration. (b) Polarization (i-V) and power density curves of H_2-O_2 and H_2-air AEMFCs employing Co/CeO_2@NC–SL as the cathode catalyst. (c) Chronoamperometric stability test of the AEMFC recorded at a constant potential of 0.70 V. (d) Comparison of the peak power density of the Co/CeO_2@NC–SL-based AEMFC with those of recently reported non-precious metal-based AEMFC cathodes.

4. Conclusions

In summary, we developed a heterostructure-engineered Co/CeO_2@NC–SL electrocatalyst with a unique 3D hexagonal star architecture for efficient bifunctional oxygen electrocatalysis. The Co/CeO_2 heterointerface acts as the intrinsic core driver of catalytic performance, inducing pronounced interfacial electron transfer and optimized electronic structure, while the CTAB-directed 3D star-like morphology serves as a crucial auxiliary framework that ensures rapid mass transport and high accessibility of active sites. Spectroscopic analyses reveal that pronounced electron transfer from Co to CeO_2 optimizes the adsorption of oxygen intermediates, thereby promoting the direct four-electron ORR pathway. Consequently, Co/CeO_2@NC–SL delivers an outstanding ORR half-wave potential of 0.87 V and a low OER overpotential of 318 mV at 10 mA cm^{-2}, along with excellent durability. The resulting rechargeable aqueous ZAB achieves a high open-circuit voltage of 1.57 V, a peak power density of 191.82 mW cm^{-2}, and ultralong cycling stability of ~1200 h, while the AEMFC delivers a peak power density of 1261.95 mW cm^{-2} under H_2-O_2 conditions. This work establishes a clear structure-interface-performance relationship and demonstrates that rational heterointerface engineering combined with morphology control is an effective strategy for designing advanced non-noble-metal bifunctional electrocatalysts for next-generation energy devices.

CRediT authorship contribution statement

Biao Fu: Writing – original draft. **Yingfang Huang:** Formal analysis, Data curation. **Peisen Wu:** Methodology, Investigation. **Ke Zhang:** Methodology, Investigation. **Zhiyang Huang:** Methodology, Investigation. **Sheraz Muhammad:** Formal analysis, Data curation. **Jiawen Huang:** Methodology, Investigation. **Jiajie Lin:** Data curation. **Tayirjan Taylor Isimjan:** Writing – review & editing. **Bao Wang:** Writing – review & editing. **Xiulin Yang:** Writing – review & editing, Supervision.

Declaration of competing interest

The authors declare that they have no known competing financial interests or personal relationships that could have appeared to influence the work reported in this paper.

Acknowledgements

This work was financially supported by the Guangxi Science and Technology Projects (GUIKELT2600640010), the Natural Science Foundation of Guangxi Province (2026GXNSFBA00640178), and the National Natural Science Foundation of China (52363028; W2621022; 21965005).

Appendix A. Supplementary data

Supplementary data to this article can be found online at https://doi.org/10.1016/j.cej.2026.184103.

Data availability

Data will be made available on request.

References

[1] Y. Li, H. Dai, Recent advances in zinc–air batteries, Chem. Soc. Rev. 43 (15) (2014) 5257–5275, https://doi.org/10.1039/c4cs00015c.
[2] J. Fu, R. Liang, G. Liu, A. Yu, Z. Bai, L. Yang, Z. Chen, Recent progress in electrically rechargeable zinc–air batteries, Adv. Mater. 31 (31) (2018) 1805230, https://doi.org/10.1002/adma.201805230.
[3] S. Ji, Y.-H. Wang, H. Liu, X. Lu, Y. Wang, X. Tian, Y. Zhao, J.H. Horton, Z. Li, Site-specific synergy by heteronuclear microenvironment atomic editing for oxygen reduction reaction, Nat. Commun. 16 (1) (2025) 11691, https://doi.org/10.1038/s41467-025-66841-2.
[4] J. Pan, Y.Y. Xu, H. Yang, Z. Dong, H. Liu, B.Y. Xia, Advanced architectures and relatives of air electrodes in Zn–air batteries, Adv. Sci. 5 (4) (2018) 1700691, https://doi.org/10.1002/advs.201700691.
[5] A. Kulkarni, S. Siahrostami, A. Patel, J.K. Nørskov, Understanding catalytic activity trends in the oxygen reduction reaction, Chem. Rev. 118 (5) (2018) 2302–2312, https://doi.org/10.1021/acs.chemrev.7b00488.
[6] Z. Li, H. Liu, Y.-H. Wang, S. Ji, Y. Zhang, Y. Liu, X. Lu, H. Teng, J.H. Horton, Y. Wang, X. Ma, Y.-J. Tang, Electronic structure modulation induced by the synergy of cobalt low-nuclearity clusters and mononuclear sites for efficient oxygen electrocatalysis, ACS Nano 19 (1) (2024) 1600–1610, https://doi.org/10.1021/acsnano.4c15035.
[7] Y. Zeng, X. Wang, W. Qi, C. Liu, L. Lu, M. Xiao, K. Li, F. Xiao, M. Shao, W. Xing, J. Zhu, Aligned d-orbital energy level of dual-atom sites catalysts for oxygen reduction reaction in anion exchange membrane fuel cells, Nat. Commun. 16 (1) (2025) 8111, https://doi.org/10.1038/s41467-025-63322-4.
[8] Z. Li, H. Liu, Y. Chen, S. Ji, X. Lu, W. Yang, Y. Wang, J.H. Horton, Y.-J. Tang, X. Tian, Modulation of d–d orbital hybridization via creating asymmetrical paired iron sites for the oxygen reduction reaction, Energy Environ. Sci. 19 (12) (2026) 3891–3909, https://doi.org/10.1039/d6ee01866a.
[9] Y. Wang, D. Wang, Y. Li, A fundamental comprehension and recent progress in advanced Pt-based ORR nanocatalysts, SmartMat 2 (1) (2021) 56–75, https://doi.org/10.1002/smm2.1023.
[10] C. Wang, L. Jin, H. Shang, H. Xu, Y. Shiraishi, Y. Du, Advances in engineering RuO_2 electrocatalysts towards oxygen evolution reaction, Chin. Chem. Lett. 32 (7) (2021) 2108–2116, https://doi.org/10.1016/j.cclet.2020.11.051.
[11] Z. Li, S. Ji, H. Liu, C. Xu, C. Guo, X. Lu, H. Sun, S. Dou, S. Xin, J.H. Horton, C. He, Constructing asymmetrical coordination microenvironment with phosphorus-incorporated nitrogen-doped carbon to boost bifunctional oxygen electrocatalytic activity, Adv. Funct. Mater. 34 (18) (2024) 2314444, https://doi.org/10.1002/adfm.202314444.
[12] H. Liu, L. Jiang, J. Khan, X. Wang, J. Xiao, H. Zhang, H. Xie, L. Li, S. Wang, L. Han, Decorating single-atomic Mn sites with FeMn clusters to boost oxygen reduction reaction, Angew. Chem. Int. Ed. 62 (3) (2023) e202214988, https://doi.org/10.1002/anie.202214988.
[13] H. Liu, L. Jiang, Y. Sun, J. Khan, B. Feng, J. Xiao, H. Zhang, H. Xie, L. Li, S. Wang, L. Han, Revisiting the role of sulfur functionality in regulating the electron distribution of single-atomic Fe sites toward enhanced oxygen reduction, Adv. Funct. Mater. 33 (35) (2023) 2304074, https://doi.org/10.1002/adfm.202304074.
[14] S. Ji, Y. Mou, H. Liu, X. Lu, Y. Zhang, C. Guo, K. Sun, D. Liu, J.H. Horton, C. Wang, Y. Wang, Z. Li, Manipulating the electronic properties of an Fe single atom catalyst via secondary coordination sphere engineering to provide enhanced oxygen electrocatalytic activity in zinc-air batteries, Adv. Mater. 36 (44) (2024) 2410121, https://doi.org/10.1002/adma.202410121.
[15] Z. Li, X. Lu, C. Guo, S. Ji, H. Liu, C. Guo, X. Lu, C. Wang, W. Yan, B. Liu, W. Wu, J. H. Horton, S. Xin, Y. Wang, Solvent-free selective hydrogenation of nitroaromatics to azoxy compounds over co single atoms decorated on Nb_2O_5 nanomeshes, Nat. Commun. 15 (1) (2024) 3195, https://doi.org/10.1038/s41467-024-47402-5.
[16] P. Yu, L. Wang, F. Sun, Y. Xie, X. Liu, J. Ma, X. Wang, C. Tian, J. Li, H. Fu, Co nanoislands rooted on co–N–C nanosheets as efficient oxygen electrocatalyst for Zn–air batteries, Adv. Mater. 31 (30) (2019) 1901666, https://doi.org/10.1002/adma.201901666.
[17] X. Xie, C. He, B. Li, Y. He, D.A. Cullen, E.C. Wegener, A.J. Kropf, U. Martinez, Y. Cheng, M.H. Engelhard, M.E. Bowden, M. Song, T. Lemmon, X.S. Li, Z. Nie, J. Liu, D.J. Myers, P. Zelenay, G. Wang, G. Wu, V. Ramani, Y. Shao, Performance enhancement and degradation mechanism identification of a single-atom co–N–C catalyst for proton exchange membrane fuel cells, Nat. Catal. 3 (12) (2020) 1044–1054, https://doi.org/10.1038/s41929-020-00546-1.
[18] D. Yan, Y. Li, J. Huo, R. Chen, L. Dai, S. Wang, Defect chemistry of nonprecious-metal electrocatalysts for oxygen reactions, Adv. Mater. 29 (48) (2017) 1606459, https://doi.org/10.1002/adma.201606459.
[19] Y. Wang, Y. Zou, L. Tao, Y. Wang, G. Huang, S. Du, S. Wang, Rational design of three-phase interfaces for electrocatalysis, Nano Res. 12 (9) (2019) 2055–2066, https://doi.org/10.1007/s12274-019-2310-2.
[20] Y. Huang, R. Yang, G. Anandhababu, J. Xie, J. Lv, X. Zhao, X. Wang, M. Wu, Q. Li, Y. Wang, Cobalt/Iron(oxides) Heterostructures for efficient oxygen evolution and benzyl alcohol oxidation reactions, ACS Energy Lett. 3 (8) (2018) 1854–1860, https://doi.org/10.1021/acsenergylett.8b01071.
[21] N. Laosiripojana, S. Assabumrungrat, Catalytic steam reforming of ethanol over high surface area CeO_2: the role of CeO_2 as an internal pre-reforming catalyst, Appl. Catal. B Environ. Energy 66 (1) (2006) 29–39, https://doi.org/10.1016/j.apcatb.2006.01.011.
[22] A. Sivanantham, P. Ganesan, S. Shanmugam, A synergistic effect of co and CeO_2 in nitrogen-doped carbon nanostructure for the enhanced oxygen electrode activity and stability, Appl. Catal. B Environ. Energy 237 (2018) 1148–1159, https://doi.org/10.1016/j.apcatb.2017.08.063.
[23] M. Li, X. Pan, M. Jiang, Y. Zhang, Y. Tang, G. Fu, Interface engineering of oxygen-vacancy-rich CoP/CeO_2 heterostructure boosts oxygen evolution reaction, Chem. Eng. J. 395 (2020) 125160, https://doi.org/10.1016/j.cej.2020.125160.
[24] M. Zhang, H. Li, J. Chen, F.-X. Ma, L. Zhen, Z. Wen, C.-Y. Xu, Transition metal (Co, Ni, Fe, Cu) single-atom catalysts anchored on 3D nitrogen-doped porous carbon nanosheets as efficient oxygen reduction electrocatalysts for Zn–air battery, Small 18 (34) (2022) 2202476, https://doi.org/10.1002/smll.202202476.
[25] H. Chang, X. Liu, S. Zhao, Z. Liu, R. Lv, Q. Zhang, T.-F. Yi, Self-assembled 3D N/P/S-tridoped carbon nanoflower with highly branched carbon nanotubes as efficient

bifunctional oxygen electrocatalyst toward high-performance rechargeable Zn-air batteries, Adv. Funct. Mater. 34 (16) (2024) 2313491, https://doi.org/10.1002/adfm.202313491.
[26] M. Liu, Q. Li, X. Xiao, Z. Xu, S. Zhang, K. Lang, B. Jing, B. Zhang, M. Ding, J. Zou, B. Jiang, Constructing co–O–Ce bridge in Mott-Schottky co/CeO_2 heterojunctions facilitates oxygen electrocatalysis bifunctionality for rechargeable Zn-air batteries, J. Energy Chem. 112 (2026) 572–583, https://doi.org/10.1016/j.jechem.2025.08.068.
[27] S. Wang, Y. Guo, Z. Zhang, Y. Zheng, Z. Zhuang, W. Yan, J. Zhang, Rare earth metal oxides tailored co-N-C catalysts for enhanced acidic oxygen reduction reaction activity and stability, Chem. Eng. J. 535 (2026) 175267, https://doi.org/10.1016/j.cej.2026.175267.
[28] L. Ye, W. Chen, Z.J. Jiang, Z. Jiang, Co/CoO heterojunction rich in oxygen vacancies introduced by O_2 plasma embedded in mesoporous walls of carbon nanoboxes covered with carbon nanotubes for rechargeable zinc–air battery, Carbon Energy 6 (7) (2024) e457, https://doi.org/10.1002/cey2.457.
[29] L. Wang, X. Hu, H. Li, Z. Huang, J. Huang, T.T. Isimjan, X. Yang, Engineering built-in electric fields in oxygen-deficient MnO-CeO_2@Cs catalysts: enhanced performance and kinetics for the oxygen reduction reaction in aqueous/flexible zinc–air batteries, Green Chem. 26 (4) (2024) 2011–2020, https://doi.org/10.1039/D3GC04537D.
[30] C. Hu, Q. Liang, Y. Yang, Q. Peng, Z. Luo, J. Dong, T.T. Isimjan, X. Yang, Conductivity-enhanced porous N/P co-doped metal-free carbon significantly enhances oxygen reduction kinetics for aqueous/flexible zinc-air batteries, J. Colloid Interface Sci. 633 (2023) 500–510, https://doi.org/10.1016/j.jcis.2022.11.118.
[31] Q. Liu, P. Qiao, M. Tong, Y. Xie, X. Zhang, K. Lin, Z. Liang, L. Wang, H. Fu, Enhancing zinc–air battery performance by constructing three-dimensional N-doped carbon coating multiple valence co and MnO heterostructures, Nano Res. 17 (6) (2024) 5104–5113, https://doi.org/10.1007/s12274-023-6404-5.
[32] Z. Zhao, C. Wang, H. Wang, Y. Shen, Q. Wang, S. Li, B. Liu, N. Zhao, C. Zhong, W. Hu, A simple way to induce anode-electrolyte interface engineering through a functional composite separator for zinc–nickel batteries, Nano Energy 97 (2022) 107162, https://doi.org/10.1016/j.nanoen.2022.107162.
[33] Y. Sun, Y. Li, S. You, X. Li, Y. Zhang, Z. Cai, M. Liu, N. Ren, J. Zou, Fe_3C/$CoFe_2O_4$ nanoparticles wrapped in one-dimensional MIL-53(Fe)-derived carbon nanofibers as efficient dual-function oxygen catalysts, Chem. Eng. J. 424 (2021) 130460, https://doi.org/10.1016/j.cej.2021.130460.
[34] X. Xu, J. Xie, B. Liu, R. Wang, M. Liu, J. Zhang, J. Liu, Z. Cai, J. Zou, PBA-derived FeCo alloy with core-shell structure embedded in 2D N-doped ultrathin carbon sheets as a bifunctional catalyst for rechargeable Zn-air batteries, Appl. Catal. B Environ. Energy 316 (2022) 121687, https://doi.org/10.1016/j.apcatb.2022.121687.
[35] W.-G. Cui, X.-Y. Zhuang, Y.-T. Li, H. Zhang, J.-J. Dai, L. Zhou, Z. Hu, T.-L. Hu, Engineering co/MnO heterointerface inside porous graphitic carbon for boosting the low-temperature CO_2methanation, Appl. Catal. B Environ. Energy 287 (2021) 119959, https://doi.org/10.1016/j.apcatb.2021.119959.
[36] M. Guo, L. Wang, Z. Huang, H. Li, T.T. Isimjan, X. Yang, Modulating the energy barrier via the synergism of Cu_3P and CoP to accelerate kinetics for bolstering oxygen Electrocatalysis in Zn-air batteries, ACS Nano 18 (27) (2024) 17901–17912, https://doi.org/10.1021/acsnano.4c04479.
[37] Z. Nie, M. Chen, L. Zhang, Q. Feng, J. Hu, X. Huang, C. Zhou, Y. Zhou, T. Wågberg, G. Hu, Tailoring the d-band center by intermetallic charge-transfer manipulation in bimetal alloy nanoparticle confined in N-doped carbon nanobox for efficient rechargeable Zn-air battery, Chem. Eng. J. 463 (2023) 142411, https://doi.org/10.1016/j.cej.2023.142411.
[38] L. Wang, J. Huang, J. Huang, B. Yao, A. Zhou, Z. Huang, T.T. Isimjan, B. Wang, X. Yang, Promoting oxygen reduction reaction kinetics through manipulating electron redistribution in CoP/Cu_3P@NC for aqueous/flexible Zn–air batteries, Green Chem. 27 (8) (2025) 2276–2285, https://doi.org/10.1039/D4GC05538A.
[39] H. Zhou, H. Liu, Y. Sun, L. Jiang, J. Xiao, H. Zhang, H. Xie, L. Li, S. Wang, L. Han, Synergistic effect of single atomic Ce sites and CeO_2 nanoparticles for boosting oxygen reduction reaction, Adv. Energy Mater. 15 (14) (2024) 2404689, https://doi.org/10.1002/aenm.202404689.
[40] M. Zhu, C. Zhao, X. Liu, X. Wang, F. Zhou, J. Wang, Y. Hu, Y. Zhao, T. Yao, L.-M. Yang, Y. Wu, Single atomic cerium sites with a high coordination number for efficient oxygen reduction in proton-exchange membrane fuel cells, ACS Catal. 11 (7) (2021) 3923–3929, https://doi.org/10.1021/acscatal.0c05503.
[41] H. Yan, N. Zhang, D. Wang, Highly efficient CeO_2-supported noble-metal catalysts: from single atoms to nanoclusters, Chem. Catal. 2 (7) (2022) 1594–1623, https://doi.org/10.1016/j.checat.2022.05.001.
[42] M. Sun, Y. Jiang, H. Song, J. Zhang, G. Yin, Y. Cui, C. Zhang, G. Yin, S. Lu, Efficient ORR facilitated by Co single atoms bridged with nitrides, Adv. Funct. Mater. 35 (34) (2025) 2504982, https://doi.org/10.1002/adfm.202504982.
[43] H. Funke, A.C. Scheinost, M. Chukalina, Wavelet analysis of extended x-ray absorption fine structure data, Phys. Rev. B 71 (9) (2005) 094110, https://doi.org/10.1103/PhysRevB.71.094110.
[44] B.B. Sarma, F. Maurer, D.E. Doronkin, J.-D. Grunwaldt, Design of Single-Atom Catalysts and Tracking Their Fate Using Operando and advanced X-ray spectroscopic tools, Chem. Rev. 123 (1) (2023) 379–444, https://doi.org/10.1021/acs.chemrev.2c00495.
[45] H. Liu, P. Li, K. Fan, F. Lu, Q. Sun, Q. Zhang, B. Li, Y. Shu, L. Zong, L. Wang, Microporous hard carbon support provokes exceptional performance of single atom electrocatalysts for advanced air cathodes, Angew. Chem. Int. Ed. 64 (23) (2025) e202501307, https://doi.org/10.1002/anie.202501307.
[46] J. Liu, C. Guo, L. Sun, Y. Liu, H. Chen, C. Shu, J. Dai, C. Xu, R. Jin, H. Li, Y. Si, Unraveling the electron transfer effect of single-metal Ce-N4 sites via mesopore-coupling for boosted oxygen reduction activity, Small 20 (4) (2023) 2305615, https://doi.org/10.1002/smll.202305615.
[47] Y. Li, Y. Qiu, Y. Wang, L. Wang, Q. Lv, Atomically asymmetrical ruthenium–oxygen–cobalt sites accelerate oxygen redox and suppress side reactions for stable lithium–oxygen batteries, ACS Nano 19 (36) (2025) 32643–32653, https://doi.org/10.1021/acsnano.5c10218.
[48] Y. Song, M. Sun, S. Zhang, X. Zhang, P. Yi, J. Liu, B. Huang, M. Huang, L. Zhang, Alleviating the work function of vein-like Co_XP by Cr doping for enhanced seawater electrolysis, Adv. Funct. Mater. 33 (30) (2023) 2214081, https://doi.org/10.1002/adfm.202214081.
[49] S. Zhao, Y. Wang, Y. Hao, L. Yin, C.-H. Kuo, H.-Y. Chen, L. Li, S. Peng, Lewis acid driving asymmetric interfacial electron distribution to stabilize active species for efficient neutral water oxidation, Adv. Mater. 36 (7) (2024) 2308925, https://doi.org/10.1002/adma.202308925.
[50] S. Zhang, C. Tan, R. Yan, X. Zou, F.-L. Hu, Y. Mi, C. Yan, S. Zhao, Constructing built-in electric field in heterogeneous nanowire arrays for efficient overall water electrolysis, Angew. Chem. Int. Ed. 62 (26) (2023) e202302795, https://doi.org/10.1002/anie.202302795.
[51] T. Wu, G. Wang, F. Zhan, Q. Dong, Q. Ren, J. Wang, J. Qiu, Surface-treated carbon electrodes with modified potential of zero charge for capacitive deionization, Water Res. 93 (2016) 30–37, https://doi.org/10.1016/j.watres.2016.02.004.
[52] Y.-H. Wang, Y. Yang, F.-Y. Gao, X.-L. Zhang, L. Zhu, H.-K. Yan, P.-P. Yang, M.-R. Gao, Unraveling stoichiometry effect in nickel-tungsten alloys for efficient hydrogen oxidation catalysis in alkaline electrolytes, Angew. Chem. Int. Ed. 63 (32) (2024) e202407613, https://doi.org/10.1002/anie.202407613.
[53] W. Zhao, W. Jia, J. Zhou, T. Zhai, Y. Wu, Z. Rana, P. Sun, Y. Liu, S. Zhou, G. Xiang, X. Wang, Nanoscale grain boundary-weakened Ce–O Covalency and surface confinement intrinsically boosting ceria surface oxygen reactivity, J. Am. Chem. Soc. 147 (15) (2025) 13050–13058, https://doi.org/10.1021/jacs.5c03536.
[54] D. Cao, Y. Mu, L. Liu, Z. Mou, S. Chen, W. Yan, H. Zhou, T.-S. Chan, L.-Y. Chang, L. Song, H.-J. Zhai, X. Fan, Axially Modified Square-pyramidal CoN_4–F_1 sites enabling high-performance Zn–air batteries, ACS Nano 18 (17) (2024) 11474–11486, https://doi.org/10.1021/acsnano.4c03261.
[55] B. Fu, W. Pan, Z. Huang, M. Gao, B. Liu, S. Muhammad, T.T. Isimjan, B. Wang, X. Yang, Realization of efficient 4e− oxygen reduction via heterojunction-phosphorus vacancy synergy for high-performance zinc–air batteries, Adv. Funct. Mater. 36 (8) (2026) e17612, https://doi.org/10.1002/adfm.202517612.
[56] K. Kim, G. Kim, T. Jeong, W. Lee, Y. Yang, B.-H. Kim, B. Kim, B. Lee, J. Kang, M. Kim, Activating the Mn single atomic Center for an Efficient Actual Active Site of the oxygen reduction reaction by spin-state regulation, J. Am. Chem. Soc. 146 (49) (2024) 34033–34042, https://doi.org/10.1021/jacs.4c13137.
[57] J. Hu, W. Shang, C. Xin, J. Guo, X. Cheng, S. Zhang, S. Song, W. Liu, F. Ju, J. Hou, Y. Shi, Uncovering dynamic edge-sites in atomic co−N−C electrocatalyst for selective hydrogen peroxide production, Angew. Chem. Int. Ed. 62 (27) (2023) e202304754, https://doi.org/10.1002/anie.202304754.
[58] X. Zhao, J. Chen, Z. Bi, S. Chen, L. Feng, X. Zhou, H. Zhang, Y. Zhou, T. Wågberg, G. Hu, Electron modulation and morphology engineering jointly accelerate oxygen reaction to enhance Zn-air battery performance, Adv. Sci. 10 (8) (2023) 2205889, https://doi.org/10.1002/advs.202205889.
[59] G. Fu, Z. Cui, Y. Chen, L. Xu, Y. Tang, J.B. Goodenough, Hierarchically mesoporous nickel-iron nitride as a cost-efficient and highly durable electrocatalyst for Zn-air battery, Nano Energy 39 (2017) 77–85, https://doi.org/10.1016/j.nanoen.2017.06.029.
[60] Y.-J. Li, L. Cui, P.-F. Da, K.-W. Qiu, W.-J. Qin, W.-B. Hu, X.-W. Du, K. Davey, T. Ling, S.-Z. Qiao, Multiscale structural engineering of Ni-doped CoO nanosheets for zinc–air batteries with high power density, Adv. Mater. 30 (46) (2018) 1804653, https://doi.org/10.1002/adma.201804653.
[61] S. Ji, Y. Wang, H. Liu, X. Lu, C. Guo, S. Xin, J.H. Horton, F. Zhan, Y. Wang, Z. Li, Regulating the electronic synergy of asymmetric atomic Fe sites with adjacent defects for boosting activity and durability toward oxygen reduction, Adv. Funct. Mater. 34 (29) (2024) 2314621, https://doi.org/10.1002/adfm.202314621.